INORGANIC CHEMISTRY FRONTIERS

CCS 中国化学会 CHINESE CHEMICAL SOCIETY

ROYAL SOCIETY OF CHEMISTRY

Octahedral morphology of NiO with (111) facet synthesized from the transformation of NiOHCl for NO_x detection and degradation: Experiment and DFT calculation

Journal:	*Inorganic Chemistry Frontiers*
Manuscript ID	QI-RES-06-2020-000682.R1
Article Type:	Research Article
Date Submitted by the Author:	16-Jul-2020
Complete List of Authors:	Hermawan, Angga; Tohoku University, Institute of Multidisciplinary Research for Advanced Material (IMRAM) Hanindriyo, Adie Tri; Japan Advanced Institute of Science and Technology Ramadhan, Erland; JAIST, School of Information Science Asakura, Yusuke; Tohoku University, Institute of Multidisciplinary Research for Advanced Materials Hasegawa, Takuya; Tohoku University, Institute of Multidisciplinary Research for Advanced Materials Hongo, Kenta; Japan Advanced Institute of Science and Technology, Research Center for Advanced Computing Infrastructure; Japan Advanced Institute of Science and Technology, School of Information Science Inada, Miki; Kyushu University, Center of Advanced Instrumental Analysis Maezono, Ryo; Japan Advanced Institute of Science and Technology, School of Information Scicnece Yin, Shu; Tohoku University, Institute of Multidisciplinary Research for Advanced Materials

ARTICLE

Octahedral morphology of NiO with (111) facet synthesized from the transformation of NiOHCl for NO_x detection and degradation: Experiment and DFT calculation†

Received 00th January 20xx,
Accepted 00th January 20xx

DOI: 10.1039/x0xx00000x

Angga Hermawan[a,§], Adie Tri Hanindriyo[b,§], Erland Rachmad Ramadhan[c], Yusuke Asakura[a], Takuya Hasegawa[a], Kenta Hongo[c,d], Miki Inada[e], Ryo Maezono[c], and Shu Yin[a,*]

Nitrogen oxides (NO_x) are poisonous gas to humans and the environment and needed to monitor at an early stage. On the other hand, facet design on metal oxide semiconductors is an efficient approach to boost their gas sensing and photocatalytic performances due to desirable active sites. However, in a rock-type structure NiO, a highly polar (111) exposed facets in NiO with rock-salt structure cannot be easily exposed due to its thermodynamically unfavorable. Herein, we demonstrate the synthesis of NiO with a dominantly (111) facet from the transformation of NiOHCl with a layered structure. Among other crystal facets, NiO-Octa (111) exhibited the best NO_x gas sensing response (16.5 %) to 300 ppb level and deNO_x photocatalytic ability over 50% under UV irradiation. The DFT calculation revealed that the abundance of Ni atoms in the clean (111) surface layer allows the favorable adsorption of N adatoms, forming the Ni-N bond. The charge transfer took place from NiO to NO orbital has proven to be a cause of bond weakening and stretching from 1.1692 Å to 1.2231 Å, leading to NO_x molecular decomposition, consistent with the experimental results.

1. Introduction

The industrialization era has brought unignorable environmental downgrade aside to economic growth and human prosperity.[1,2] Air quality worsening, one of the serious environmental issues caused by automotive engine and industrial exhaust gases has become an utmost concern for scientists, engineers, and environmentalists due to their effect on human health and surrounding eco-system.[3] For instance, Nitrogen oxides, NO_x, are deadly atmospheric contaminants produced from hydrocarbons combustion processes such as vehicle engines or power plants which usually occur at high temperature.[3–5] Not to mention electrical generation from non-renewable fuels, the massive use of vehicles, especially in the metropolitan city, has made the condition is getting worse by the time.[6] Hence, there is an urgent need for the development of highly responsive and active photocatalyst materials towards NO_x detection and degradation, respectively, for environmental pollution control. In addition, a single material that can be applied in multiple applications is desirable for technological simplicity.[7]

Many different kinds of NO_x sensor and photocatalyst materials have been extensively studied, especially semiconductor metal oxides (SMOX) owing to their tailorable physical and chemical properties.[3,8–13] Due to these, SMOX exhibits a very promising and outstanding performance alongside with reversibility and long term stability. Nickel Oxide (NiO), is a rock-salt type metal oxides and well-known p-type semiconductor metal oxides for multifunctionality of environmentally benefit applications such as photocatalyst and sensor for the hazardous gas. [11,14,15] However, NiO wide-bandgap value ranging from 3.6 to 4.0 eV has set drawbacks which may limit its NO_x sensor responsivity and photocatalytic activity.[16] Various approaches have been attempted to design a high-performance semiconductor photocatalyst and sensor, involving morphological control, atomic doping incorporation, and surface defect engineering.[17–19] Precise control of exposed facets has been proven to be advantageous for the improved performance of sensor and photocatalyst nanocrystals and even more versatile than specific surface area, porosity, and other influencing factors.[20,21] Desired exposed facet can provide a highly energetic and active site through high-density of low-coordinated atoms for selective molecular adsorption.[21] The facet selective property hinders the material to adsorb undesired molecules target from the surrounding environment, leading to an exceptional activity for sensors and photocatalyst.

As a typical rock-salt structure, NiO has three thermodynamically favorable crystal facets, *e.g.* (100), (110),

[a] *Institute of Multidisciplinary research for Advanced Materials (IMRAM), Tohoku University 2-1-1 Katahira, Aoba-ku, Sendai, Miyagi 980-8577, Japan*
[b] *School of Materials Science, JAIST, Asahidai 1-1, Nomi, Ishikawa, 923-1292, Japan*
[c] *School of Information Science, JAIST, Asahidai 1-1, Nomi, Ishikawa, 923-1292, Japan*
[d] *Research Center for Advanced Computing Infrastructure, JAIST, Asahidai 1-1, Nomi, Ishikawa 923-1292, Japan*
[e] *Center of Advanced Instrumental Analysis, Kyushu University, 6-1 Kasuga-Koen, Kasuga-Shi, Fukuoka 816-8580, Japan*

† Electronic Supplementary Information (ESI) available: [details of any supplementary information available should be included here]. See DOI: 10.1039/x0xx00000x

§ The authors are equally contributed

and (111). (100) facet, specifically, has the lowest formation energy and is the most stable form thermodynamically.[22] Thus, molecular adsorption onto NiO (100) facet has been done in the majority of the previous investigation.[23] However, with the development of the materials synthesis method, it is potentially possible to design a rock-salt type material with dominantly (110) and (111) facets.[23] Mesopores NiO with (110) facet has been successfully obtained by a post-treatment of β-$Ni(OH)_2$.[24] CoO with (111) facet can be directly prepared by calcination of $CoCl_2$ precursor.[25] Other studies also show the preparation of MgO (111) facets via the inexpensive wet chemical method.[26] These investigations showed the formation of exposed facet of rock-salt crystals, including NiO, is largely dependent on synthesis conditions such as initial precursors, or ligands. While NiO can be prepared through the calcination of β-$Ni(OH)_2$ at elevated temperatures at around 400 °C to preserve the morphology of the parent β-$Ni(OH)_2$,[11,27] there is still limited knowledge on the phase and morphological transformation to NiO from other starting material.

In this work, we present a newly developed route to synthesize NiOHCl, a layered structure hydroxychloride, as a potential precursor to produce NiO with highly polar exposed (111) facet. In all investigations to date, NiOHCl has not been transformed to NiO,[28–31] although its layer structure holds a promise to be translated into rock salt structure and Cl^- in its structure may stabilize the polar (111) facet through electrostatic stabilization during the transformation.[32] NO_x gas sensing property and photocatalytic ability of NiO (111) facet were superior to NiO (110) facet obtained by annealing of β-$Ni(OH)_2$ for which the DFT *ab initio* calculation revealed that Bridge site in (111) facet is the most favourable place for NO_x adsorption. The Crystal Orbital Hamilton Population (COHP) was utilized to deeply understand the physical origin of how the adsorption and charge transfer mechanism from NiO to the molecular orbital of NO_x occurred which led to NO_x decomposition.

2. Experimental

All the chemicals in the experiments were purchased from FUJIFILM Wako Pure Chemicals Corporation, analytical grade, and utilized without additional treatment.

2.1 Preparation of NiOHCl hexagonal plate and NiO (111) octahedral morphology

The hexagonal morphology of nickel hydroxychloride (NiOHCl) was synthesized by a water-controlled release solvothermal process (WCRSP).[33] 77.8 mg of anhydrous Nickel (II) Chloride ($NiCl_2$) was dissolved into 50 mL of 1-propanol (1-PrOH) anhydrous with vigorous stirring with a constant speed of 500 rpm for 25 min at RT. Then, 10 mL of anhydrous acetic acid (AcOH) followed by the same stirring condition. The resulting solution was transferred to 100 mL Teflon lined-autoclaved and solvothermally treated at 200 °C for 10 h. After cooled to room temperature, the light green powder was recovered by a vacuum-filtration, dried at 60 °C, and ground by mortar. Finally, to obtain NiO with octahedral morphology, the obtained NiOHCl was calcined at 400 °C for 3 h. The sample was named as NiO Octa-(111).

2.2 Synthesis of NiO (110) hexagonal morphology

Hexagonal morphology of NiO with (110) exposed facet was produced by following the previous report.[24] 0.02 mol of anhydrous $NiCl_2$ was dissolved in 10 mL of DI water followed by the addition of 6 M NaOH under the stirring condition. Then, 0.6 mmol of sodium sulfate (Na_2SO_4) was added into the solution. After transferring to Teflon-lined autoclave with 100 mL capacity, the solution was treated at 170 °C for 24 h. The green $Ni(OH)_2$ product was collected by vacuum filtration and dried at 60 °C. Then, it was finally calcined at 400 °C for 3 h to obtain the NiO-Hexa (110) sample.

2.3 Characterizations

X-ray diffraction (XRD, Bruker AXS D2 PHASER with CuKα radiation = 1.5418 Å) employed to identify the phase of the obtained samples. Morphological features and structural parameters were observed by Field emission scanning electron microscopy (FE-SEM, Hitachi S4800) and transmission electron microscopy (TEM, JEOL JEM–2010, and Topcon EM-002B). The chemical state, composition, and bonding were characterized by X-ray photoelectron spectroscopy (XPS, ULVAC PHI5600). Non-metallic elements such as H, C, O, and Cl in the prepared samples were measured by elemental analysis. Thermogravimetric-differential thermal analysis (TG–DTA, Rigaku ThemoPlus TG 8120) was utilized to determine phase transformation and weight loss of the nickel hydroxychloride (NiOHCl) precursor. Optical properties were collected using UV–vis spectroscopy (JASCO V-670 Spectrophotometer) and Photoluminescence spectra (JASCO FP-8500 Spectrofluorometer). The specific surface area was calculated through the BET method from N_2 isotherm measurement (Quantachrome, NOVA 4200e). The solvent mixture after the solvothermal reaction of NiOHCl was analyzed by nuclear magnetic resonance (1H NMR, Varian Unity Inova, 500 MHz).

2.4 DFT Calculation

Density Functional Theory (DFT) calculations are performed with plane-wave basis sets and periodic boundary conditions, using the slab model to simulate surface conditions. Generalized Gradient Approximation (GGA) exchange-correlation functionals parametrized by Perdew, Burke, and Ernzerhof (PBE)[34] are chosen along with appropriate Hubbard U correction for NiO to produce a more accurate electronic structure for Mott insulators.[35] The effective Hubbard U parameter for NiO has been thoroughly explored and tested in earlier works. Parameter values of U_{eff} = U-J = 5.3 eV, with U = 6.3 eV and J = 1 eV is chosen according to a previous investigation of water adsorption on NiO (100]) surface[36] and other, earlier investigations into NiO.[35,37,38] Core electrons are treated with the projector-augmented wave (PAW) method.[39] Calculations are performed with the Vienna Ab Initio Simulation Package (VASP) software package.[40–43]

Visualization of crystal structures, both for input and output of first-principles calculations, is performed with the Visualization for Electronic and Structural Analysis (VESTA) program.[44] The detail regarding calculation parameters on NiO facets and NO_x adsorption can be found in the electronic supplementary information (ESI).†

Distinguishing the contribution of hybridized orbitals to interatomic bonding is key to analyzing binding or adsorption between two systems. In this way, Crystal Orbital Hamilton Population (COHP) analysis is an effective tool in distinguishing bonding and antibonding orbitals resulting from hybridization between two atoms. In the theoretical portion of this work, we employ the Local Orbital Basis Suite Towards Electronic Structure Reconstruction (LOBSTER) code which applies the projected COHP (pCOHP) method to extract similar atom resolved chemical information from wavefunctions with plane-wave basis sets.[45–48] The pCOHP method projects the plane-wave basis set representation of the wavefunction onto atomic orbital-like contributions to the molecular orbitals, from which a more chemical picture may be shown.

2.5 Gas sensing and photocatalytic evaluation

To fabricate the sensor device, 0.010 g of the obtained NiO samples were mixed with ethanol to obtain a slurry which then was brush-coated onto an Au interdigitated electrode (IDE). The gas sensing evaluation for the obtained material was conducted using a home-built electrical measurement system (Agilent Keysight 34970A) with 2 probe method at various temperatures from room temperature to 300 °C to mimic the challenging condition of automobile engine exhaust system. The variation of temperatures is critical to determine the optimum working temperature of the sensor device for the real application. It is noteworthy to mention that to minimize the photocatalytic effect of NiO, our sensing equipment used a metal chamber with an insignificant possibility of light to irradiate the samples. The sensing response (R) was calculated by following formula $R(\%) = ((R_g-R_a)/R_a) \times 100$ % where R_g is resistance in targeting gas and Ra is the resistance in ambient air. The response and recovery times were also assessed by calculating the time needed to reach a 90 % variation of saturated resistance during the injection and rejection of testing gas, respectively.

The photocatalytic degradation of NO_x ($deNO_x$) towards NiO octahedral and hexagonal was evaluated in a flow-type reactor at room temperature. The samples were placed throughout the dent (20 mm × 16 mm × 0.5 mm) of a glass plate holder and this holder was then placed in the middle of the reactor. A mercury lamp with a power of 450 W was utilized as a light source and two different filters (λ> 510 nm and >400 nm) were applied to investigate photocatalytic activity in Visible and UV-region. NO_x analyzer (Yanaco, ECL-88A) was employed to measure the NO_x concentration. The flow rate of NOx gas was adjusted to 200 mL/min.

3. Result and discussion

3.1 Crystal structure and morphology characterization

Fig. 1 (a) shows XRD patterns of NiOHCl and β-$Ni(OH)_2$ precursors. For NiOHCl, the 003 plane located at 15.6° was very intense compared to 012, 015, 009, 107, and 110 planes centered at 33.3°, 41.3°, 48.0 °, 49.4 °, and 56.5°, respectively. To determine the quality of the crystal structure of the NiOHCl sample, Rietveld analysis was employed using RIETAN-FP software.[49] As shown in **Fig. S1** (a), the Rietveld refinement assuming the rhombohedral structures (space group $\overline{R3}m$) has converged resulting in a lattice parameters of a = 3.2674 Å, c = 17.068 Å R_{wp} (%) = 3.977, R_p (%) = 2.428, R_e (%) = 0.646 and S = 6.1596. The goodness-of-fit, S, was very large due to XRD profile of NiOHCl has a high base line. The refined results for structural parameters was summarized in **Table S2**. Additionally, the Ni-O and Ni-Cl bonding distances are 2.036(6) Å and 2.453(5) Å, respectively. Due to the disorder behaviour of anion site, average bond distance of $Ni[(OH),Cl]_6$ is 2.036(6) ~ 2.453(5) Å.

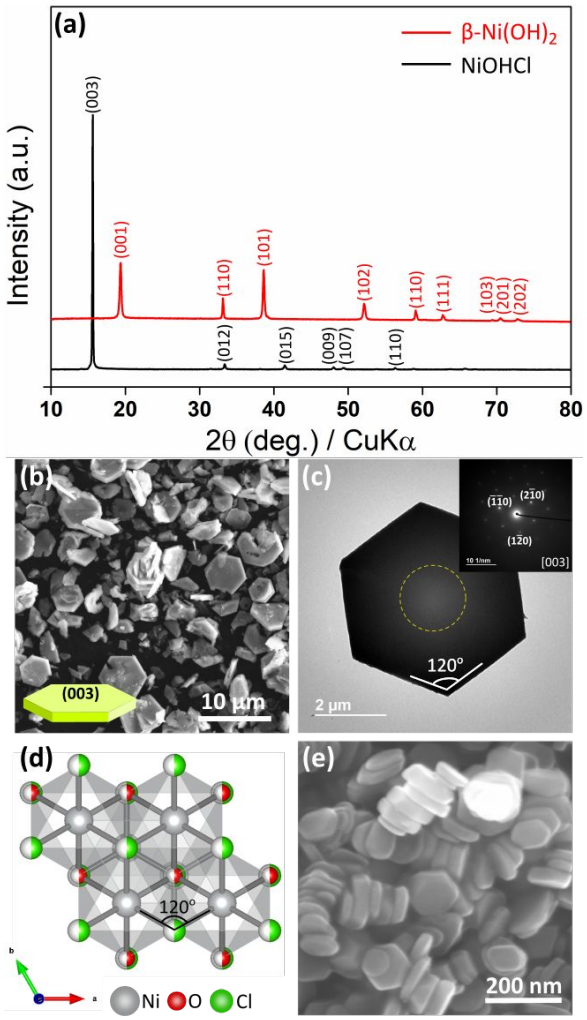

Fig. 1 (a) XRD pattern of NiOHCl and β-$Ni(OH)_2$, (b) SEM image (c) TEM image (inset is SAED pattern taken from area indicated by a dashed-line circle) (d) crystal structure of NiOHCl along the (003) facet showing oxygen and chlorine atoms possess other atom occupancies and (e) SEM image of β-$Ni(OH)_2$

Comparing to earlier study (summarized in **Table S3**),[29] NiOHCl sample in this work has a slightly higher structural parameter value, suggesting a structural expansion (**Fig. S1** (b)) which might be attributed to a small organic molecules incorporation, revealed by CHN analysis (C= 2.6 wt.%, H = 3.95 wt.% and O=17.34 wt.%) Meanwhile, the emerged peaks of β-Ni(OH)$_2$ were in a good agreement with the standard (PDF card 14-0117).

Morphology and particle size of NiOHCl and β-Ni(OH)$_2$ phases were observed by SEM and TEM. As revealed by the SEM and TEM images in **Fig. 1 (b)** and **(c)**, NiOHCl has a nearly perfect hexagonal morphology with the size of approx. 5 μm, angle of 120° at each corner, and acceptable homogeneity although some split particle was observed. From the corresponding selected area electron diffraction (SAED) pattern taken from the yellow circle area, the hexagonal NiOHCl exhibited a single crystalline property (inset of **Fig. 1** (c)) with ($\bar{1}\,\bar{1}$0), (2$\bar{1}$0), and (1 $\bar{2}$0) planes from [003] zone axis. This may indicate the electron beam is perpendicular with (003) facet of hexagonal morphology as well NiOHCl crystal structure. It is reasonable considering the (003) facet of the NiOHCl crystal structure refined by the Rietveld analysis (**Fig. 1 (d)**) clearly shows that the hexagonal morphology with an angle of 120°. Furthermore, TG/DTA and elemental analysis were utilized to provide further insight into the stoichiometric and phase transformation of NiOHCl. From the TG-DTA measurement (**Fig. S2**), the weight loss of NiOHCl was 36.4 wt. % due to the evaporation of HCl, leading to the transformation into the NiO phase based on the following reaction: NiOHCl → NiO + HCl. The weight loss is very close to the theoretical molecular weight of HCl (36.4 wt. %). Additionally, the elemental analysis confirmed the Cl amount in NiOHCl was 36.57 wt. % that agreed with an atomic mass of Cl (35.4 wt. %). Thus, the formation of NiOHCl is fully convincing based on the result above. The obtained β-Ni(OH)$_2$ phase also shows a similar hexagonal structure with a smaller particle size (ca. 150 nm). Based on the previous investigation, the hexagonal morphology of β-Ni(OH)$_2$ possessed (001) exposed facet with a high ratio to the total surface.[24]

It is widely known that the formation pathway of β-Ni(OH)$_2$ involved the hydrolysis of nickel salt precursors. However, the formation of NiOHCl in organic solvents is not well-investigated. Thus, it is of foremost importance to understand the chemical reactions involved in the formation of the NiOHCl phase. Herein, we performed ^{1}H NMR analysis to elucidate the chemical composition of solvents after the solvothermal process and propose the reaction pathway accordingly. Detail explanation can be found in ESI.† It seems that NiOHCl also undergoes a hydrolysis reaction, but it is limited by the amount of generated water molecules from the esterification reaction. However, we could not obtain either NiOHCl or β-Ni(OH)$_2$ phase when the solution was changed from mixed 1-PrOH/AcOH to distilled (DI) water. It may imply that NiOHCl was preferably formed in the acidic condition rather than in the neutral condition. This also supports earlier studies.[28–30]

The XRD patterns of NiO obtained from the calcination of NiOHCl and β-Ni(OH)$_2$ were shown in **Fig. 2** (a). Regardless the precursors' phase, the well-defined peaks appeared at 37.2, 43.2, 62.8, 75.3, 79.3° correspond to the (111), (200), (220), (311) and (222) of cubic structures NiO with a monoclinic phase which agreed to standard (PDF Card 47-1049). The obtained NiO was also a pure phase proven by no observed impurities peak. Textural coefficient (TC) can determine the preferred orientation of a material. TC is calculated as:[25]

$$\mathrm{TC(hkl)} = \frac{\mathrm{I}(hkl)/\mathrm{I_o}(hkl)}{\frac{1}{N}\sum \mathrm{I}(hkl)/\mathrm{I_o}(hkl)}$$

where $\mathrm{I}(hkl)$ is the intensity of the (hkl) obtained from XRD measurement, $\mathrm{I_o}(hkl)$ is the diffraction intensity of the NiO according to the PDF card 47-1049 , and N is the number of diffraction peaks used in the calculation. Any material with a random crystal orientation, the TC should be 1. We obtained that the TC(111) fo NiO-Octa (111) and NiO-Hexa (110) are 1.110 and 0.985, a strong indication of more (111) preferred orientation in NiO-Octa (111) than that in NiO-Hexa (110).

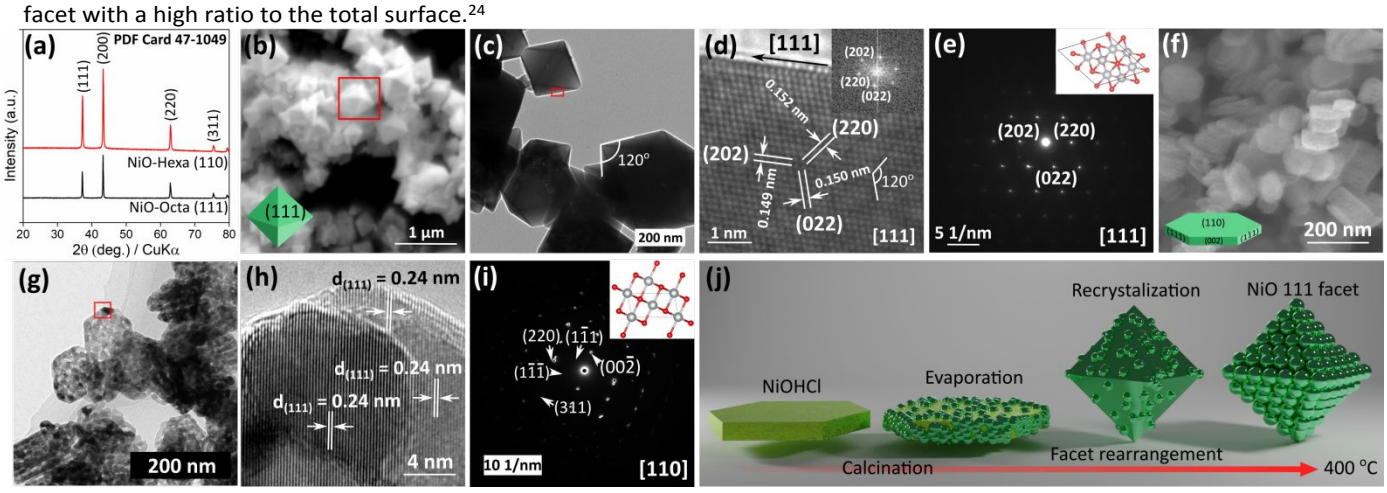

Fig. 2 (a) XRD patterns of the NiO Octa (111) and NiO Hexa (110), (b) SEM, (c) TEM, (d) HRTEM (inset is FFT), (e) SAED pattern taken from red area (inset is corresponding crystal structure with cut-off in [111] zone axis) of NiO-Octa (111) sample. (f) SEM, (g) TEM, (h) HRTEM, (i) SAED pattern taken from red area (inset is corresponding crystal structure with cut-off in [110] zone axis) of NiO-Hexa (110) sample. (j) a simplified illustration of morphological transformation of NiOHCl hexagonal into NiO octahedral.

As can be seen in SEM and TEM images (**Fig. 2** (b)-(c)), after the calcination at 400 °C, the hexagonal morphology of NiOHCl was drastically transformed into octahedral morphology with dominantly exposed (111) facet on the geometrical system. Inclusive of nanosized particles (100-500 nm), the octahedral morphology of NiO (111) exhibited a smooth surface. **Fig. 2** (d) displayed high-resolution TEM (HRTEM) shows the lattice distance of 0.149 nm, 0.150 nm, and 0.153 nm attributed to d-spacing of 202, 022, and 220, respectively, very close to reports from Kim and co-workers.[27] Moreover, the corresponding Fast-Fourier-Transform (FFT) pattern (**Fig. 2 (d)**, inset), and selected area diffraction pattern (SAED) depicted in **Fig. 2 (e)** suggests that NiO with octahedral morphology is single-crystalline. All FFT and SAED spots can be indexed along [111] zone axis of octahedral NiO. These results demonstrated that (111) plane (**Fig. 2** (e), inset) is parallel with the surface of NiO octahedral morphology, revealing the dominant facet is (111). All characterization results agreed to the previous reports of NiO 111 facet. On the contrary, the NiO morphology and particle size obtained from β-$Ni(OH)_2$ precursor were identical with the parent hexagonal morphology (SEM, **Fig. 2** (f)). Nonetheless, due to the evaporation of H_2O, the NiO hexagonal morphology showed a mesoporosity architecture (TEM, **Fig. 2** (g)). Although it possesses the porous structure that may induce the formation of another facet, only one d-lattice spacing was observed (0.24 nm) which is attributed to (111) crystal plane. However, the amount of another possible facet such as (002), ($11\bar{1}$), and ($1\bar{1}$ 1), however, the (110) facet is still dominant as its amount is more than 66% revealed by the previous study.[24] The SAED pattern shown in **Fig. 2** (h) implies the single-crystalline nature of NiO hexagonal morphology from which the indexed planes indicate the [110] zone axis is concurrent with the TEM incident beam and parallel with the top surface of NiO hexagonal morphology. The above results confirmed NiO hexagonal morphology has dominantly (110) exposed facet and were consistent with the reproduced report.[22] From now on, the NiO samples in this study were labeled as NiO-Octa (111) and NiO-Hexa (110).

An interesting phenomenon on how dramatical change on the morphology after the calcination occurs should be investigated. Thus, it is also noteworthy to reveal the transformation mechanism from NiOHCl hexagonal to NiO octahedral morphology with (111) facet by varying calcination temperatures while taking XRD and SEM measurement at each temperature. As can be seen in **Fig. S4** (a), almost no alteration in the XRD patterns after the calcination up to 350 °C, demonstrating NiOHCl phase stability under 400 °C, being consistent with TG/DTA. Only at 400 °C, full phase transformation has occurred. This also indicates that no intermediate chemical was formed. In **Fig. S4** (b), SEM images showed the morphological transformation of NiOHCl. The hexagonal morphology can still be observed even at 350 °C. However, it was broken up into a very fine crystal due to the start of HCl evaporation. TEM image (**Fig. S4** (c)) reveals that octahedral nanostructures have already formed within the porous hexagonal morphology at this temperature. Therefore, it might conclude that the evaporation-recrystallization-facet arrangement process has simultaneously occurred. The simplified illustration of the structural transformation is displayed in **Fig. 2** (j).

The subsequent investigation is how NiO (111) facet could form in the case of NiOHCl, but could not in β-$Ni(OH)_2$ case. Both precursors possess similar layer structures. The only difference is that the existence of Cl^- and OH^- in NiOHCl and β-$Ni(OH)_2$, respectively. There is a possibility that Cl^- served as a capping agent to the Ni^{2+} during the calcination process as Ni atom is abundant in the clean (111) surface layer. Moreover, Ni atom in (111)-terminated surfaces exhibited a positive charge (+1.37) based on the previous investigation.[50] It is likely that Cl-attached to and coordinated with Ni by electronic interaction and it may inhibit the growth of NiO in the (111) direction. The Cl ligand-capped (111) facet can also be found in the CoO case which has the same rock-salt structure.[25] The NiO octahedral morphology was also obtained by heating the irregular particle of $NiCl_2$ precursor at 400 °C at ambient pressure for 3 h inside a covered crucible similar to that of NiOHCl calcination. **(Fig. S5)** Nevertheless, the pure NiO phase was not obtained in such conditions, revealing that (i) Cl^- can assist the (111) facet formation, (ii) pre-existed oxygen in NiOHCl phase may be helpful to acquire the pure phase and (iii) facet rearrangement may occur at the nanoscale interface. Recent work also reveals NiO with several exposed facets ({311}, {611}, {100} and {111}) can be achieved, from nickel salt precursors, only by the aid of anion and alkali cation of molten salts.[51] This may support our hypothesis.

3.2 Electronic and optical properties

X-ray photoelectron spectroscopy analysis was employed to explore the chemical composition and oxidation state of Octahedral NiO (111) facet. The full survey spectrum indicates a distinct chemical element of Ni and O and a tiny peak of Cl (**Fig. S6 (a)**). EDX-equipped SEM elemental scanning (**Fig. S6 (b)**) taken from Fig. 3 (b) also suggested the presence of Ni and O. **Fig. 3 (a)** displays Ni 2p core-level spectra. Using the Gaussian fitting function within Shirley background, it was deconvoluted into two spin doublets positioned at 856.3 eV (Ni $2p_{3/2}$) and 874.1 eV (Ni $2p_{1/2}$) and two shake-up satellites (862.4 eV and 879.6 eV). The fitting peaks at binding energies of 856.7 eV and 874.0 eV were attributed to Ni^{2+} state, while other fitting peaks located at 854.0 eV and 871 eV are ascribed to Ni^{3+} state.[52–54] The existence of doublets of Ni 2p together with their satellite confirmed the magnetic chemical state in Ni^{2+} and Ni^{3+}.[55] The formation of Ni^{3+} might be attributed to O-rich nickel oxides.[56] However, other phrases related to Ni^{3+} were negligible as only pure NiO is detected in XRD patterns. The Cl content was confirmed to be 0.74 wt.% by elemental analysis. **Fig. 3(b)**

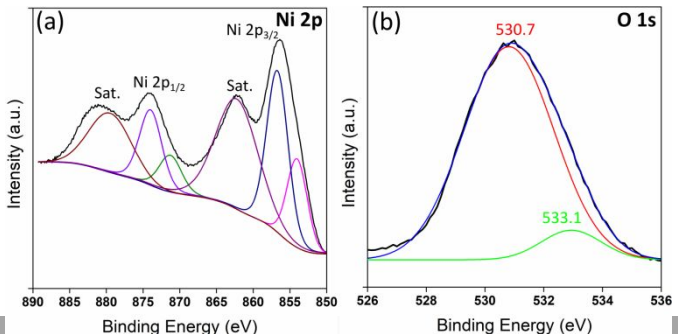

Fig. 3 XPS core level spectra of (a) Ni 2p and (b) O 1s of NiO-Octa (111).

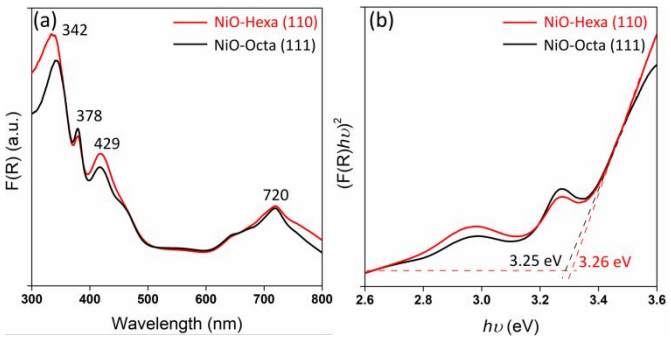

Fig. 4 (a) Kubelka-Munk Absorption spectra and (b) corresponding Tauc plot of NiO Hexa (110) and NiO Octa (111)

displayed O1s core spectra that were deconvoluted using gaussian fitting. The peak at 530.7 is a typical metal bond with oxides, and fitting peak emerged at 533.1 eV may be attributed to physically adsorbed water molecules at surface, since it was found that NiO with 111-exposed facet is water molecule sensitive.[57,58]

The optical properties of the obtained NiO were further scrutinized. The UV-Vis absorption of octahedral NiO in the Kubelka-Munk unit is depicted in **Fig. 4 (a)**. As can be seen, the two samples have similar emerged peaks. The sharp peak at the UV region (342 nm) can be assigned to bandgap absorption of NiO, while other three broad absorption edges at 378 nm, 429 nm, and 720 nm are a typical d-d transition existed within the bandgap of NiO with Ni^{2+} state that is surrounded six O^{2-} at the octahedral site. This octahedral configuration splits d-electron of ground state $^3A_{2g}$ to $1E_g$, $^3T_{2g}(G)$, and $^3T_{1g}(F)$, respectively.[59–61] Then, employing the Tauc-method to the KM absorption spectra, the estimated bandgap for NiO Octa (111) and NiO Hexa (110) were 3.26 and 3.25 eV (**Fig. 4 (b)**). This result suggests that Cl impurity in NiO Octa (111) does not infer the electronic band structures.

3.3 NO_x gas sensing properties and DeNO_x photocatalytic activity

The NiO with a polycrystalline property without specific exposed facet was also synthesized for comparison. The synthesis process was the same as that of NiO-Octa (111), except the nonexistence of acetic acid during WCRSP. As illustrated in **Fig. S7** (a-d), the XRD pattern, TEM, HRTEM, and SAED confirmed the formation of NiO phase that has irregular morphology, the lattice fringe of 0.21 nm ($d_{(200)}$) and 0.245 nm ($d_{(111)}$) and a diffuse ring of polycrystalline material. Thus, this sample is denoted as NiO-irregular. Also, UV-Vis DRS (**Fig. S7** (e), shows similar characteristic with other two samples. Moreover, the Cl content was 0.70 wt.%, very close to that of NiO-Octa (111).

The sensor devices containing NiO samples with distinctive morphology and exposed face, namely NiO-Octa (111), NiO-Hexa (110), and NiO irregular were tested at different temperatures from room temperatures to 300 °C toward NO_x gas detection. The concentration of NO_x was determined to 3 ppm. As depicted in **Fig. 5** (a), the sensing response of NiO

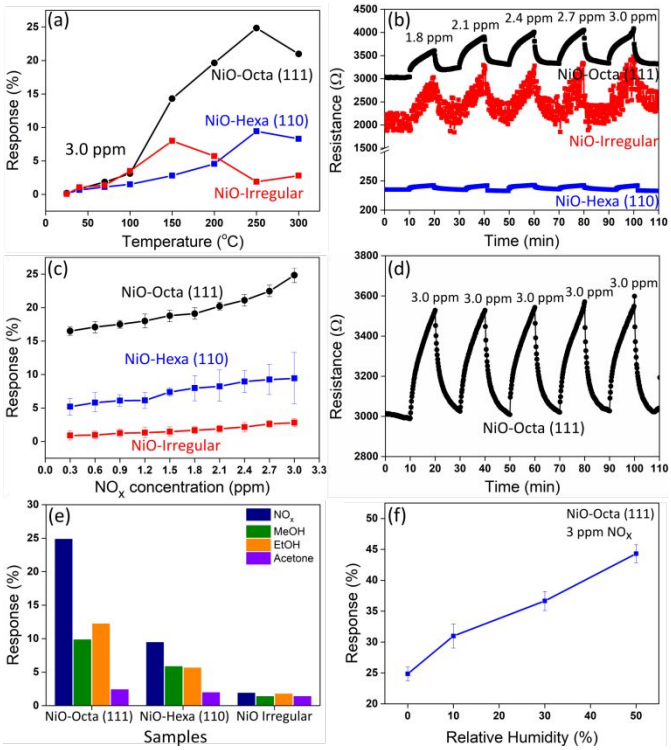

Fig. 5 (a) Temperature dependent NO_x gas sensing properties, (b) NO_x concentration-dependent responses at 250 °C, (c) response *vs* NO_x concentration of the synthesized NiO samples; (d) repeatability response under 3 ppm of NOx gas of NiO-Octa (111) sample; selectivity of NiO samples under 3 of different gases and (e) NO_x response of NiO-Octa (111) under different relative humidity.

samples increased with the rise of operating temperature. All NiO samples exhibited a mountain hill feature from which the optimum operating condition can be determined.This characteristic is influenced mainly by the adsorption-desorption process. As practically proposed, NiO-Octa (111) sample may be more suitable as an integrated gas sensing material in the vehicle combustion system for real-time pollution monitoring. The NO_x response of NiO-Octa (111) at 250 °C was 24.85 %, which is about 3 times higher than that of NiO-Hexa (110) (9.34 %) and 13 times higher than NiO-Irregular (1.9 %). **Fig. 5** (b) shows the transient response/recovery feature of NiO-Octa (111), NiO-Hexa (110), and NiO-Irregular underexposure of NO_x with a concentration range of 1.8 ppm to 3.0 ppm. All samples manifest similar response/recovery times where the resistance increased upon the exposure of NO_x. However, the NiO-Irregular demonstrated a strong noise in contrary to NiO-Octa (111) and NiO-Hexa (110). The noise may be due to a low or unstable adsorption/desorption process. Also, the different base resistance, *e.g.* the resistance in air atmosphere, observed on all samples indicated the dependency of electrical resistance on particle size or impurities .[62] It is clear that the gas responses of NiO-Octa (111), NiO-Hexa (110) and NiO-Irregular linearly increase with the NO_x concentration as displayed in **Fig. 5** (c). Specifically for the case of NiO-Octa (111), it still has good response value (16.5%) even to 300 ppb of NO_x exposure, which is a substantial indication of NiO-Octa (111) potentiality for low-limit detection of NO_x gas. Moreover, under 3 ppm of NOx at 250 °C the response/recovery features of NiO-Octa (111) are repeatable for at least 5 times with no obvious changes in the

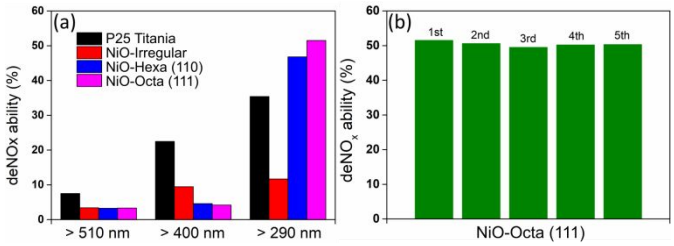

Fig. 6 (a) NO_x conversion of P25 titania and the obtained NiO samples under different wavelength, and (b) stability of NiO Octa (111) towards $deNO_x$ photocatalytic after five runs.

electrical resistance during the NO_x injection and ejection. These repeatability features are a very crucial parameter of gas sensing materials for long-term use. **Fig. 5** (e) depicted gas sensing response of NiO samples under 3 ppm of various gases e.g. Nitrogen Oxides (NO_x), Methanol (MeOH), Ethanol (EtOH) and Acetone. NiO-Octa (111) sample possessed a highly selective properties to NO_x gas indicated by the degree of selectivity ($R_{NOx}/R_{othergas}$) is above 2. The NO_x sensing response of NiO-Octa (111) under different relative humidity (RH) was futher studied because most of oxides are also sensitive to moisture. As shown in **Fig. 5** (f), the response of NiO-Octa (111) to NO_x increased as the RH increased. It is may likely NiO-Octa (111) also strongly adsorbed the water molecules that increase the resistance, in line with reported literature.[57] NiO-Octa (111) NO_x dynamic response was repeatable for several consecutive days (**Fig. S8)**, reflecting its good stability against such dynamic condition.

We further investigated the $deNO_x$ photocatalytic ability of all NiO samples. **Fig. 6 (a)** shows NO_x conversion of NiO-Octa (111), NiO-Hexa (110), and NiO irregular accompanied with that of commercial P25 titania photocatalyst where the samples were irradiated with different wavelength (>510 nm, >400 nm, and >290 nm). Even though the NiO-Octa (111) exhibited inferior photocatalytic activity in the visible-light irradiation (>510 nm, and >400 nm), the NO_x conversion of about 50 % was achieved in the UV regions exceeding P25 titania, NiO-Hexa (110), and NiO-Irregular. This result indicated that even though NiO exhibited a wide bandgap (3.25 eV), the visible light induced photocatalytic activity can still be achieved due to d-d transition in a typical metal transition element which acts as trapping state to promote a narrower bandgap and prolong the recombination rate.[63] On the other hand, when the irradiation energy was sufficient to excite electrons from valence bands, the activity was very different from each other. This result means the crystal facet plays a crucial role in the photocatalytic reaction. It is confirmed from N_2 measurement, the BET specific surface areas (SSA) of NiO-Octa (111), NiO-Hexa (110), NiO-Irregular, and P25 titania are 14.1 m^2/g, 62.7 m^2/g, 18.3 m^2/g, and 50.6 m^2/g, respectively. Therefore, those greater specific surface areas do not have a large contribution to the $deNO_x$ activity. **Fig. 6 (b)** displays the stability of the NO_x conversion of NiO-Octa (111) with >290 nm light irradiation. NiO-Octa (111) has a stable performance of NO_x conversion after five runs, demonstrating its stability under UV-light. One may question that Cl may influence gas sensing and photocatalytic properties. Nevertheless, with similar Cl content, NiO-Octa (111) and NiO Irregular showed distinctive performance. Thus, Cl may give a minor contribution to the superior performance of NiO-Octa (111).

3.4 DFT calculation, gas sensing, and photocatalyst mechanism

To investigate the adsorption mechanism of NO on the NiO surface, *ab initio* calculations are performed. We have successfully prepared two facets, (110) and (111). Therefore, these facets together with a naturally formed (100) facet. Furthermore, it is useful to consider the electronic structure of the NO molecule as the adsorbate in question. **Fig. S9** (a) shows a rough molecular orbital diagram for NO, specifically for the resultant hybrid orbitals from the N and O 2p orbitals. It can be seen that one electron occupies the $\pi*$ antibonding orbital, with the rest of the $\pi*$ antibonding orbitals empty just above the Fermi level. It then follows by analyzing the projected COHP (pCOHP) of the N-O bond after adsorption and comparing it with the rough diagram for the NO molecule, it is possible to see the effects of NO adsorption on the N-O molecular antibonding orbitals. This comparison can also shed light on the mechanism of NO adsorption during gas sensing and photocatalytic process.

The combination of possible adsorption sites and adsorbate conformation generates a series of conformations as shown in **Fig. S9** (b). The horizontal orientation of the adsorbate (NO bond parallel to the surface) is likely to occur at the bridge site with two bonds to the surface, while vertical or tilted orientation is possible on either top, hollow, or bridge sites. Some conformations are more energetically favorable than others, lowering the adsorption energy associated. The adsorption energy is defined as the energy required for adsorption to occur and is mathematically defined as:

$$E_{ads} = E_{tot} - E_{surface} - E_{mol} \qquad \text{(Eq. 1)}$$

where E_{ads} denotes the adsorption energy, E_{tot} denotes the total energy of the adsorbed system, $E_{surface}$ the total energy of the slab model, and E_{mol} the total energy of the adsorbate (molecule) in a vacuum. This mathematical definition is akin to binding or cohesive energy, and it represents the strength of adsorption.

From the selected calculation results as summarized in **Table I** (full results can be found in **Table S4**), it can be observed that bridge site adsorption is particularly favorable for NO in NiO (100) surface, especially with the nitrogen adatom. Two of the striking results are from conformations 31_BridN and 33_BridPar, both of which include a (relatively) stronger Ni-N bond and the oxygen in NO adsorbate elevated at some distance from the surface. NO adsorption on NiO (100) surface of the adsorbate results in a tilted end position of NO molecule, suggesting that NO is adsorbed in a tilted conformation for all sites on NiO (100). These results agree well with previous theoretical works on NiO (100) surfaces[36,64] which predict that adsorptions of oxygen gas and water vapor on NiO (100) often

rely instead on defects (oxygen vacancies) present in the surface. The calculation results indicate that it is likely that the pure NiO (100) surface is not favorable for the adsorption of NO as well. The weak adsorption energies on (100) facet suggest that it is not a good surface for use in gas sensing and photocatalyst application, which confirms one part of the facet-selective property of NiO surfaces.

As with the (100) facet, the (110) surface facet is nonpolar, containing both Ni and O atoms. Its surface energy is roughly in between the (100) and (111) facets, and it has 3 different bridge sites: between the Ni atoms, between the O atoms, and between one Ni and one O atom. Calculations are done for 3 adsorbate conformation ("vertical", horizontal, and parallel) for the three bridge sites. The adsorption energies again show that NO adsorbs with N adatom instead of O, that the Ni-N bond is most significant, and that the bridge and hollow sites are most favourable, producing the strongest adsorption. It also shows that NO adsorption is generally more favourable towards this (110) surface compared to the (100) surface.

Table I. NO adsorption on NiO (100), (110) and (111) surfaces

Surface	Conformation	E_{ads} (eV)
(100)	31_BridN	-0.458
	33_BridPar	-0.423
(110)	21_HolN	-1.231
	31_BridNiNiN	-1.248
(111)	11_TopN	-2.345
	23_HolHCP	-2.429
	31_BridN	-2.395

The (111) surface facet of NiO is comprised of alternating layers of Ni and O atoms in the close-packed structure. By far the (111) surface shows the most favorable sites for NO adsorption, again for the hollow and bridge sites with a tilted NO conformation, continuing the trend from (110) surface. Again, the Ni-N bond seems to be of significant importance, as seen in the prominence of adsorption on Ni top, bridge, and hollow sites compared with the rest, with the strongest adsorption at the hollow HCP site (**Fig. S9** (b) and **Fig. 7**). This pattern closely resembles that of the (110) surface, with even stronger adsorption energies. The calculated results confirm the facet selectivity property of the NiO surface, from the (111) surface is being most favorable toward NO adsorption, to (110), and lastly to the (100) surface producing the weakest adsorption.

The increased favourability in adsorption is easily attributable to the abundance of Ni atoms in the clean (111) surface layer (Ni-terminated). O-terminated (111) surface is not investigated in this work, but from the previous results, it can be safely extrapolated that such a surface would not be favored toward NO adsorption. For nearly all cases, N-O or O-O adsorption is far weaker in comparison with the Ni-N adsorption, which effectively rules out the O-terminated (111) surface as favorable towards NO adsorption compared to Ni terminated (111) surface.

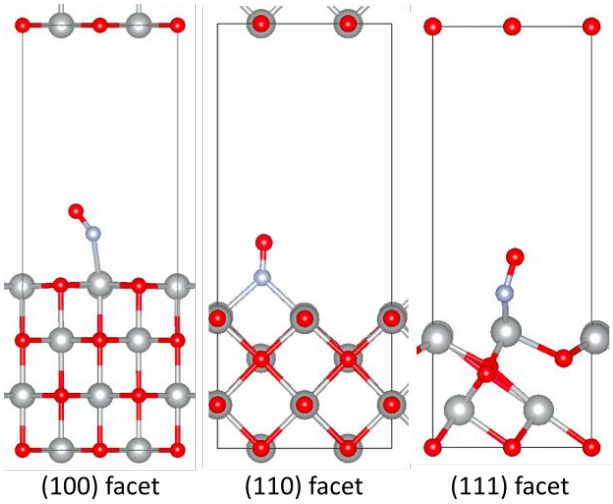

Fig. 7 xz-plane views of optimized geometries for 31_BridN site in (100) facet, 31_BridNiNiN site in (110) facet, and 31_BridN site in (111) facet, showing significant Ni-N bond and tilted conformation of adsorbate (NO molecule).

To reveal the mechanism of NO adsorption in NiO Octa (111), the 31_BridN site is taken as an example, with a significant adsorption energy and a clear adsorption between adatom N and single surface Ni atom. The plane-wave basis set wavefunction is projected onto atomic orbital like contributions to the molecular orbitals by the projected COHP method. At the same time, the density of states (DOS) and projected DOS (PDOS) information are also extracted from a single-point

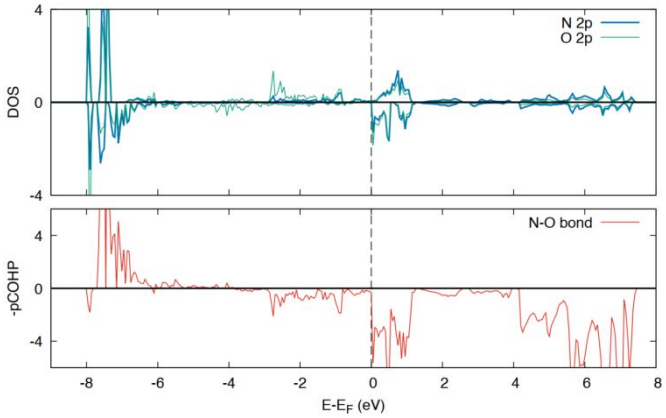

Fig. 8 PDOS and pCOHP plots of the adsorbate (NO) for 31_BridN site in (111) facet case. pCOHP plot is inversed to follow the chemistry convention of presenting bonding orbitals on positive axis of plot.

calculation of the adsorbed system. **Fig. 8** shows the PDOS of the 2p orbitals of both N and O atoms from the adsorbate as well as the pCOHP analysis of the N-O bond. The $\pi*$ orbital just below the Fermi surface (seen in **Fig. S9** (a)) has been delocalized, stretching to up to 3 eV below the Fermi level. This shows the increased occupation of the antibonding orbital because of a small charge transfer from the NiO surface, which is likely considering the difference in electronegativity between Ni and N atoms. Therefore, NO adsorption onto the NiO surface likely occurs by a small charge transfer from the surface to the N atom. The above mechanism produces an expectation of a

weakening N-O bond, due to the occupation of the $\pi*$ antibonding orbital. This is easy to achieve considering that the orbital in question is both the HOMO and LUMO levels of the NO molecule at the same time. Geometry optimization precisely shows this effect, with post-adsorption N-O bond length stretched to 1.2231 Å from the initial bond length 1.1692 Å (in a vacuum). The stretching of the bond length suggests a weakening in the N-O bond and provides evidence of adsorption by charge transfer from the NiO surface. It agreed with the increased resistance of NiO, regardless of the exposed facet, during the exposure of NO gas. This mechanism also explains the importance of Ni surface atoms as adsorption sites considering the electronegativity of Ni as opposed to O atoms. It explains the significance of Ni-N bonding as well as the trend of adsorption strength dependence on the surface facet of NiO, from (111) > (110) > (100). The DFT calculation was also conducted to reveal the good selectivity of NiO with (111) facet. The methanol, ethanol, and acetone molecules were place on Hollow HCP site (HolHCP) of (111) plane. The calculated adsorption energies were -1.083, -1.182, -1.002 eV, -0.505 eV, -1.811 eV for methanol, ethanol, acetone, hydrogen and ammonia, respectively. This prediction by theoretical calculation tracks well with the experimental results.

4. Conclusion

In summary, NiO with dominantly exposed facets, (110) and (111), were successfully obtained by the calcination of different precursors. The Cl^- ion from NiOHCl precursor may hypothetically assist the crystal growth and lower the formation energy of (111) surface facet. This sample, NiO Octa (111), exhibited the best NO_x gas sensing response (24.85%) at 250 ^oC and $DeNO_x$ photocatalytic activity over 50 % under UV irradiation, exceeding all examined samples. The *ab initio* calculation revealed that the NO gas is likely to be adsorbed on Ni terminated surface with N adatom rather than O. The NO adsorption energy was -0.458, -1.248, and -2.429 eV on NiO with (100), (110), and (111) facet, respectively, well-agreed with the experimental results. The charge transfer occurred from NiO to NO, promoting the increased internal resistance in NiO and weakening the N-O bonding. The above combination of experimental and calculation results demonstrates that the surface-engineering approach offers the potential to design high-performance gas sensing and photocatalyst materials.

Acknowledgments

A.H, T.H., Y.A., R.M., M.I., and S.Y. acknowledged the funding from Japan Society for the Promotion of Science (JSPS) Grant-in-Aid for the Scientific Research (KAKENHI) on Innovative Areas “Mixed Anion” (No. 16H06439, 16H06440, 19H04692), and Grants Number (20H00297). A.H, T.H., Y.A., and S.Y., are grateful for the financial support from The Dynamic Alliance for Open Innovations Bridging Human, Environment and Materials, the Cooperative Research Program of “Network Joint Research Center for Materials and Devices!” A.T.H. is grateful for financial supports from MEXT-KAKENHI (JP16K21724). R.M. is grateful for financial supports from MEXT-KAKENHI (17H05478 and 16KK0097), from FLAGSHIP2020 (project nos. hp180206 and hp180175 at K-computer), from Toyota Motor Corporation, from I-O DATA Foundation, and the Air Force Office of Scientific Research (AFOSR-AOARD/FA2386-17-1-4049). K.H. is grateful for financial supports from KAKENHI grant (19K05029) and a Grant-in-Aid for Scientific Research on Innovative Areas (16H06439 and 19H05169). The computation in this work has been performed using the facilities of the Research Center for Advanced Computing Infrastructure (RCACI) at JAIST.

Author Contribution

A.H. designed and conducted the experiments and wrote the manuscript.
A.T.H planned and executed the DFT simulation and wrote the manuscript.
E.R.R involved in the plan and discussion of DFT simulation
T.H., Y.A., S.Y., M.I., K.H., and R.M. supervised, checked, and revised the manuscript.

Notes and references

1 K. Wetchakun, T. Samerjai, N. Tamaekong, C. Liewhiran, C. Siriwong, V. Kruefu, A. Wisitsoraat, A. Tuantranont and S. Phanichphant, Semiconducting metal oxides as sensors for environmentally hazardous gases, *Sensors Actuators, B Chem.*, 2011, **160**, 580–591.

2 J. Cherniwchan, Economic growth, industrialization, and the environment, *Resour. Energy Econ.*, 2012, **34**, 442–467.

3 N. Miura, T. Koga, M. Nakatou, P. Elumalai and M. Hasei, Electrochemical NOx sensors based on stabilized zirconia: Comparison of sensing performances of mixed-potential-type and impedancemetric NO_x sensors, *J. Electroceramics*, 2006, **17**, 979–986.

4 A. Afzal, N. Cioffi, L. Sabbatini and L. Torsi, NO_x sensors based on semiconducting metal oxide nanostructures: Progress and perspectives, *Sensors Actuators, B Chem.*, 2012, **171–172**, 25–42.

5 J. Liao, Z. Li, G. Wang, C. Chen, S. Lv and M. Li, ZnO nanorod/porous silicon nanowire hybrid structures as highly-sensitive NO_2 gas sensors at room temperature, *Phys. Chem. Chem. Phys.*, 2016, **18**, 4835–4841.

6 B. Son, W. Yang, P. Breysse, T. Chung and Y. Lee, Estimation of occupational and nonoccupational nitrogen dioxide exposure for Korean taxi drivers using a microenvironmental model, *Environ. Res.*, 2004, **94**, 291–296.

7 E. G. C. Neiva, M. M. Oliveira, M. F. Bergamini, L. H. Marcolino and A. J. G. Zarbin, One material, multiple functions: Graphene/$Ni(OH)_2$ thin films applied in batteries, electrochromism and sensors, *Sci. Rep.*, 2016, **6**, 1–14.

8 C. Guo, X. Wu, M. Yan, Q. Dong, S. Yin, T. Sato and S. Liu, The visible-light driven photocatalytic destruction of NO_x using mesoporous TiO_2 spheres synthesized via a ‘water-controlled release process’, *Nanoscale*, 2013, **5**, 8184–

8191.

9 T. yang Wang, Y. yuan Li, T. tian Li, H. Yu, Y. Yang, H. Yang and X. T. Dong, Enhanced NO_x gas sensing properties of Cr_2O_3 film modified ordered porous ZnO gas sensors, *Solid State Ionics*, 2018, **326**, 173–182.

10 J. Ma, H. Wu, Y. Liu and H. He, Photocatalytic removal of NO_x over visible light responsive oxygen-deficient TiO_2, *J. Phys. Chem. C*, 2014, **118**, 7434–7441.

11 Q. Dong, S. Yin, C. Guo, X. Wu, N. Kumada, T. Takei, A. Miura, Y. Yonesaki and T. Sato, Single-crystalline porous NiO nanosheets prepared from β-$Ni(OH)_2$ nanosheets: Magnetic property and photocatalytic activity, *Appl. Catal. B Environ.*, 2014, **147**, 741–747.

12 S. Yin, Creation of advanced optical responsive functionality of ceramics by green processes, 2015, 823–834.

13 S. Yin and Y. Asakura, Recent research progress on mixed valence state tungsten based materials, *Tungsten*, 2019, **1**, 5–18.

14 H. J. Kim and J. H. Lee, Highly sensitive and selective gas sensors using p-type oxide semiconductors: Overview, *Sensors Actuators, B Chem.*, 2014, **192**, 607–627.

15 N. D. Hoa and S. A. El-Safty, Synthesis of mesoporous NiO nanosheets for the detection of toxic NO_2 gas, *Chem. - A Eur. J.*, 2011, **17**, 12896–12901.

16 B. Sasi, K. G. Gopchandran, P. K. Manoj, P. Koshy, P. Prabhakara Rao and V. K. Vaidyan, Preparation of transparent and semiconducting NiO films, *Vacuum*, 2002, **68**, 149–154.

17 H. Tong, S. Ouyang, Y. Bi, N. Umezawa, M. Oshikiri and J. Ye, Nano-photocatalytic materials: Possibilities and challenges, *Adv. Mater.*, 2012, **24**, 229–251.

18 A. Mikolajczyk, A. Malankowska, G. Nowaczyk, A. Gajewicz, S. Hirano, S. Jurga, A. Zaleska-Medynska and T. Puzyn, Combined experimental and computational approach to developing efficient photocatalysts based on Au/Pd-TiO_2 nanoparticles, *Environ. Sci. Nano*, 2016, **3**, 1425–1435.

19 T. Li, Z. Shen, Y. Shu, X. Li, C. Jiang and W. Chen, Facet-dependent evolution of surface defects in anatase TiO_2 by thermal treatment: Implications for environmental applications of photocatalysis, *Environ. Sci. Nano*, 2019, **6**, 1740–1753.

20 M. H. Huang and P. H. Lin, Shape-controlled synthesis of polyhedral nanocrystals and their facet-dependent properties, *Adv. Funct. Mater.*, 2012, **22**, 14–24.

21 J. Pal and T. Pal, Faceted metal and metal oxide nanoparticles: Design, fabrication and catalysis, *Nanoscale*, 2015, **7**, 14159–14190.

22 A. Wander, I. J. Bush and N. M. Harrison, Stability of rocksalt polar surfaces: An ab initio study of MgO(111) and NiO(111), *Phys. Rev. B - Condens. Matter Mater. Phys.*, 2003, **68**, 1–4.

23 C. A. Cadigan, A. R. Corpuz, F. Lin, C. M. Caskey, K. B. H. Finch, X. Wang and R. M. Richards, Nanoscale (111) faceted rock-salt metal oxides in catalysis, *Catal. Sci. Technol.*, 2013, **3**, 900–911.

24 D. Su, M. Ford and G. Wang, Mesoporous NiO crystals with dominantly exposed {110} reactive facets for ultrafast lithium storage, *Sci. Rep.*, 2012, **2**, 1–7.

25 B. Liu, L. Ma, L. C. Ning, C. J. Zhang, G. P. Han, C. J. Pei, H. Zhao, S. Z. Liu and H. Q. Yang, Charge separation between polar {111} surfaces of CoO octahedrons and their enhanced visible-light photocatalytic activity, *ACS Appl. Mater. Interfaces*, 2015, **7**, 6109–6117.

26 Z. Li, C. V. Ciobanu, J. Hu, J. P. Palomares-Báez, J. L. Rodríguez-López and R. Richards, Experimental and DFT studies of gold nanoparticles supported on MgO(111) nano-sheets and their catalytic activity, *Phys. Chem. Chem. Phys.*, 2011, **13**, 2582–2589.

27 C. W. Kim, Y. S. Son, A. U. Pawar, M. J. Kang, J. Y. Zheng, V. Sharma, P. Mohanty and Y. S. Kang, Facile fabrication and photoelectrochemical properties of a one axis-oriented NiO thin film with a (111) dominant facet, *J. Mater. Chem. A*, 2014, **2**, 19867–19872.

28 K. He, G. Zhao and G. Han, Synthesis of nickel hydroxychloride microspheres via a facile template-free process and their conversion to β-$Ni(OH)_2$ microspheres, *CrystEngComm*, 2014, **16**, 11050–11057.

29 S. Hu and X. Wang, Fullerene-like colloidal nanocrystal of nickel hydroxychloride, *J. Am. Chem. Soc.*, 2010, **132**, 9573–9575.

30 S. Fu, L. Li, Y. Zhang, S. Chen, S. Fang, Y. Jing and G. Li, Anion De/Intercalation in Nickel Hydroxychloride Microspheres: A Mechanistic Study of Structural Impact on Energy Storage Performance of Multianion-Containing Layered Materials, *ACS Appl. Energy Mater.*, 2018, **1**, 1522–1533.

31 S. H. Lim, G. D. Park, D. S. Jung, J. H. Lee and Y. C. Kang, Towards an efficient anode material for Li-ion batteries: Understanding the conversion mechanism of nickel hydroxy chloride with Li-ions, *J. Mater. Chem. A*, 2020, **8**, 1939–1946.

32 H. Zhang, B. M. May, J. Serrano-Sevillano, M. Casas-Cabanas, J. Cabana, C. Wang and G. Zhou, Facet-Dependent Rock-Salt Reconstruction on the Surface of Layered Oxide Cathodes, *Chem. Mater.*, 2018, **30**, 692–699.

33 A. Hermawan, Y. Asakura, M. Inada and S. Yin, One-step synthesis of micro-/mesoporous SnO_2 spheres by solvothermal method for toluene gas sensor, *Ceram. Int.*, 2019, **45**, 15435–15444.

34 J. P. Perdew, K. Burke and M. Ernzerhof, Generalized gradient approximation made simple, *Phys. Rev. Lett.*, 1996, **77**, 3865–3868.

35 S. Dudarev and G. Botton, Electron-energy-loss spectra and the structural stability of nickel oxide: An LSDA+U study, *Phys. Rev. B - Condens. Matter Mater. Phys.*, 1998, **57**, 1505–1509.

36 N. Yu, W. B. Zhang, N. Wang, Y. F. Wang and B. Y. Tang, Water adsorption on a NiO(100) surface: A GGA+U study, *J. Phys. Chem. C*, 2008, **112**, 452–457.

37 G. Rohrbach, J. Hafner and G. Kresse, Molecular adsorption on the surface of strongly correlated transition-metal oxides: A case study for CO/NiO(100), *Phys. Rev. B -*

Condens. Matter Mater. Phys., 2004, **69**, 1–13.

38 W. B. Zhang, Y. L. Hu, K. L. Han and B. Y. Tang, Pressure dependence of exchange interactions in NiO, *Phys. Rev. B - Condens. Matter Mater. Phys.*, 2006, **74**, 3–7.

39 P. E. Blöchl, Projector augmented-wave method, *Phys. Rev. B*, 1994, **50**, 17953–17979.

40 G. Kresse and J. Hafner, Ab initio molecular dynamics for liquid metals, *Phys. Rev. B*, 1993, **47**, 558–561.

41 G. Kresse and J. Hafner, Ab initio molecular-dynamics simulation of the liquid-metalamorphous- semiconductor transition in germanium, *Phys. Rev. B*, 1994, **49**, 14251–14269.

42 G. Kresse and J. Furthmüller, Efficiency of ab-initio total energy calculations for metals and semiconductors using a plane-wave basis set, *Comput. Mater. Sci.*, 1996, **6**, 15–50.

43 G. Kresse and J. Furthmüller, Efficient iterative schemes for ab initio total-energy calculations using a plane-wave basis set, *Phys. Rev. B - Condens. Matter Mater. Phys.*, 1996, **54**, 11169–11186.

44 K. Momma and F. Izumi, VESTA 3 for three-dimensional visualization of crystal, volumetric and morphology data, *J. Appl. Crystallogr.*, 2011, **44**, 1272–1276.

45 V. L. Deringer, A. L. Tchougréeff and R. Dronskowski, Crystal orbital Hamilton population (COHP) analysis as projected from plane-wave basis sets, *J. Phys. Chem. A*, 2011, **115**, 5461–5466.

46 R. Dronskowski and P. E. Blöchl, Crystal orbital hamilton populations (COHP). Energy-resolved visualization of chemical bonding in solids based on density-functional calculations, *J. Phys. Chem.*, 1993, **97**, 8617–8624.

47 S. Maintz, V. L. Deringer, A. L. Tchougréeff and R. Dronskowski, Analytic projection from plane-wave and PAW wavefunctions and application to chemical-bonding analysis in solids, *J. Comput. Chem.*, 2013, **34**, 2557–2567.

48 S. Maintz, V. L. Deringer, A. L. Tchougréeff and R. Dronskowski, LOBSTER: A tool to extract chemical bonding from plane-wave based DFT, *J. Comput. Chem.*, 2016, **37**, 1030–1035.

49 F. Izumi and K. Momma, Three-dimensional visualization in powder diffraction, *Solid State Phenom.*, 2007, **130**, 15–20.

50 N. Erdman, O. Warschkow, D. E. Ellis and L. D. Marks, Solution of the p(2 × 2) NiO(111) surface structure using direct methods, *Surf. Sci.*, , DOI:10.1016/S0039-6028(00)00860-8.

51 M. D. Susman, H. N. Pham, X. Zhao, D. H. West, S. Chinta, P. Bollini, A. K. Datye and J. D. Rimer, Synthesis of NiO Crystals Exposing Stable High-Index Facets, *Angew. Chemie Int. Ed.*, 2020, **59**, 1–6.

52 C. Yuan, J. Li, L. Hou, X. Zhang, L. Shen and X. W. Lou, Ultrathin mesoporous $NiCo_2O_4$ nanosheets supported on Ni foam as advanced electrodes for supercapacitors, *Adv. Funct. Mater.*, 2012, **22**, 4592–4597.

53 C. Long, M. Zheng, Y. Xiao, B. Lei, H. Dong, H. Zhang, H. Hu and Y. Liu, Amorphous Ni-Co Binary Oxide with Hierarchical Porous Structure for Electrochemical Capacitors, *ACS Appl. Mater. Interfaces*, 2015, **7**, 24419–24429.

54 S. Chen, G. Yang, Y. Jia and H. Zheng, Three-dimensional $NiCo_2O_4$@$NiWO_4$ core-shell nanowire arrays for high performance supercapacitors, *J. Mater. Chem. A*, 2017, **5**, 1028–1034.

55 P. Dubey, N. Kaurav, R. S. Devan, G. S. Okram and Y. K. Kuo, The effect of stoichiometry on the structural, thermal and electronic properties of thermally decomposed nickel oxide, *RSC Adv.*, 2018, **8**, 5882–5890.

56 M. S. Jo, S. Ghosh, S. M. Jeong, Y. C. Kang and J. S. Cho, Coral-Like Yolk–Shell-Structured Nickel Oxide/Carbon Composite Microspheres for High-Performance Li-Ion Storage Anodes, *Nano-Micro Lett.*, 2019, **11**, 1–18.

57 W. Zhao, M. Bajdich, S. Carey, A. Vojvodic, J. K. Nørskov and C. T. Campbell, Water dissociative adsorption on NiO(111): Energetics and structure of the hydroxylated surface, *ACS Catal.*, 2016, **6**, 7377–7384.

58 M. A. Peck and M. A. Langell, Comparison of nanoscaled and bulk NiO structural and environmental characteristics by XRD, XAFS, and XPS, *Chem. Mater.*, 2012, **24**, 4483–4490.

59 M. Lenglet, F. Hochu, J. Dürr and M. H. Tuilier, Investigation of the chemical bonding in 3d8 nickel(II) charge transfer insulators (NiO, oxidic spinels) from ligand-field spectroscopy, Ni 2p XPS and X-ray absorption spectroscopy, *Solid State Commun.*, 1997, **104**, 793–798.

60 Y. Qi, H. Qi, J. Li and C. Lu, Synthesis, microstructures and UV-vis absorption properties of β-$Ni(OH)_2$ nanoplates and NiO nanostructures, *J. Cryst. Growth*, 2008, **310**, 4221–4225.

61 Y. Cui, C. Wang, S. Wu, G. Liu, F. Zhang and T. Wang, Lotus-root-like NiO nanosheets and flower-like NiO microspheres: Synthesis and magnetic properties, *CrystEngComm*, 2011, **13**, 4930–4934.

62 A. Mirzaei, J. H. Kim, H. W. Kim and S. S. Kim, How shell thickness can affect the gas sensing properties of nanostructured materials: Survey of literature, *Sensors Actuators, B Chem.*, 2018, **258**, 270–294.

63 S. Shen, J. Chen, X. Wang, L. Zhao and L. Guo, Microwave-assisted hydrothermal synthesis of transition-metal doped $ZnIn_2S_4$ and its photocatalytic activity for hydrogen evolution under visible light, *J. Power Sources*, 2011, **196**, 10112–10119.

64 J. M. McKay and V. E. Henrich, Surface electronic structure of NiO: Defect states, O_2 and H_2O interactions, *Phys. Rev. B*, 1985, **32**, 6764–6772.